Microscale anthropogenic pollution modelling in a small tropical island during weak trade winds: Lagrangian particle dispersion simulations using real nested LES meteorological fields

Raphaël Cécé, Didier Bernard, Jérôme Brioude, Narcisse Zahibo

Atmospheric Environment 139 (2016) 98–112

Contents lists available at ScienceDirect

Atmospheric Environment

journal homepage: www.elsevier.com/locate/atmosenv

Microscale anthropogenic pollution modelling in a small tropical island during weak trade winds: Lagrangian particle dispersion simulations using real nested LES meteorological fields

Raphaël Cécé [a, *], Didier Bernard [a], Jérome Brioude [b, c], Narcisse Zahibo [a]

[a] LaRGE, Department of Physics, University of the French West Indies, Pointe-à-Pitre, Guadeloupe
[b] Cooperative Institute for Research in Environmental Sciences, University of Colorado, Boulder, USA
[c] LACy (UMR 8105/Université de La Réunion, CNRS, Météo-France), La Réunion, France

HIGHLIGHTS

- Numerical simulation of a severe NO_x pollution case over the Guadeloupe archipelago.
- WRF-LES-FLEXPART used with a microscale downscaling (1 km, 333 m and 111 m).
- Forward simulations of a power plant plume showed good agreement with observations.
- Need of the LES scheme to predict NO_x concentrations in the turbulence grey zone.
- Backtrajectories identified realistic sources of NO_x in the urban area.

ARTICLE INFO

Article history:
Received 30 December 2015
Received in revised form
11 May 2016
Accepted 14 May 2016
Available online 15 May 2016

Keywords:
FLEXPART-WRF
Large-Eddy simulation
Tropical island
Air dispersion modelling
Power plant NO_x
Source identification

ABSTRACT

Tropical islands are characterized by thermal and orographical forcings which may generate microscale air mass circulations. The Lesser Antilles Arc includes small tropical islands (width lower than 50 km) where a total of one-and-a-half million people live. Air quality over this region is affected by anthropogenic and volcanic emissions, or saharan dust. To reduce risks for the population health, the atmospheric dispersion of emitted pollutants must be predicted. In this study, the dispersion of anthropogenic nitrogen oxides (NO_x) is numerically modelled over the densely populated area of the Guadeloupe archipelago under weak trade winds, during a typical case of severe pollution. The main goal is to analyze how microscale resolutions affect air pollution in a small tropical island. Three resolutions of domain grid are selected: 1 km, 333 m and 111 m. The Weather Research and Forecasting model (WRF) is used to produce real nested microscale meteorological fields. Then the weather outputs initialize the Lagrangian Particle Dispersion Model (FLEXPART). The forward simulations of a power plant plume showed good ability to reproduce nocturnal peaks recorded by an urban air quality station. The increase in resolution resulted in an improvement of model sensitivity. The nesting to subkilometer grids helped to reduce an overestimation bias mainly because the LES domains better simulate the turbulent motions governing nocturnal flows. For peaks observed at two air quality stations, the backward sensitivity outputs identified realistic sources of NO_x in the area. The increase in resolution produced a sharper inverse plume with a more accurate source area. This study showed the first application of the FLEXPART-WRF model to microscale resolutions. Overall, the coupling model WRF-LES-FLEXPART is useful to simulate the pollutant dispersion during a real case of calm wind regime over a complex terrain area. The forward and backward simulation results showed clearly that the subkilometer resolution of 333 m is necessary to reproduce realistic air pollution patterns in this case of short-range transport over a complex terrain area. Globally, this work contributes to enrich the sparsely documented domain of real nested microscale air pollution modelling. This study dealing with the determination of the proper resolution grid and proper turbulence scheme, is of significant interest to the near-source and complex terrain air quality research community.

* Corresponding author. LaRGE, Department of Physics, University of the French West Indies, Fouillole Campus, Pointe-à-Pitre 97110, Guadeloupe.
E-mail address: raphael.cece@univ-ag.fr (R. Cécé).

http://dx.doi.org/10.1016/j.atmosenv.2016.05.028

1. Introduction

Tropical islands are mostly characterized by strong solar radiation, sea/land thermal contrast and complex topography. These thermal and mechanical forcings may generate mesoscale and microscale air mass circulations (Carlis et al., 2010; Jury et al., 2009; Lefèvre et al., 2010; Lesouëf et al., 2011; Matthews et al., 2007; Oliphant et al., 2001; Yang and Chen, 2005; Yu et al., 2014). Orographical effects of islands on impinging synoptic flow may be coarsely predicted by the local Froude number Fr (U/Nh), with U the wind speed, N the buoyancy frequency and h the maximum height. The Lesser Antilles Arc includes small tropical islands (width lower than 50 km) which separate the Atlantic Ocean from the Caribbean Sea. A total of one-and-a-half million people live in this area extending from Grenada (12.12° N, 61.68° W) to the Virgin Islands (18.34° N, 64.93° W). Low topography islands ($Fr \geq 1$) like Barbados induce air-mass circulations, such as land-sea breezes and convective circulations, mainly driven by thermal contrasts (Mahrer and Pielke, 1976; Whitehall et al., 2013; Jähn et al., 2015). Mountainous islands ($Fr < 1$) like St-Vincent, Dominica and Montserrat induce air-mass circulations, such as blocking on windward slopes and calm wind area on the leeward coast, mainly driven by mechanical effects (Smith et al., 1997, 2012; Poulidis et al., 2016). These orographically/thermally induced airflows occurring at meso- and micro-scale must be studied to understand the mechanisms which drive dispersion and transport of air pollutants in the atmospheric boundary layer of these small islands.

Air quality over the Lesser Antilles islands is affected by multiple sources: anthropogenic emissions, volcano plumes and fumaroles, saharan dust, sargassum seaweed (H2S gas released). Apart from the large-scale origin of saharan dust and the regional-scale origin of volcanic eruption plumes, all major sources are local, linked with different island-scale wind regimes: inland, orographical, coastal, windward and leeward. In the focused area, the most important anthropogenic sources are generation of electric power and transport activities. The electricity of the Lesser Antilles islands is mainly generated by coal and diesel power plants which induce permanent pollutant gas plumes. The terrain complexity (topography, coastline and land-use) and the small distance between potential industrial sources and residential areas located at less than 2 km would suggest the need for subkilometer meteorological fields to well reproduce the main governing factors of air pollution: transport driven by local flows and dispersion driven by shear/buoyancy production.

Real numerical weather simulations including dynamical downscaling from large-scale to mesoscale resolution (100−1 km) are numerous in the literature (Carlis et al., 2010; Cécé et al., 2014; Jury et al., 2009; Lefèvre et al., 2010; Madalaa et al., 2015; Nguyen et al., 2010; Seaman et al., 2012; Srinivas et al., 2015; Whitehall et al., 2013; Yang and Chen, 2005). Most of these numerical studies are made with the Weather Research and Forecasting model (WRF; Skamarock et al. (2008)). These real nested mesoscale simulations associated with 1D ensemble-mean turbulence schemes, have shown their good ability to reproduce the main features of regional meteorological phenomena. Downscaling from meso- to micro-scale (<1 km) resolution associated with 3D Large Eddy Simulation scheme, is recent. The nesting from an 1D ensemble-mean turbulence scheme to Large-Eddy 3D closure scheme is at this stage sparsely documented (Mirocha and Kirkil, 2010; Mirocha et al., 2014; Muñoz-Esparza et al., 2014). Most studies dealing with this topic have been made with the coupled model WRF-LES which simulated realistic microscale meteorological variable fields (Chu et al., 2014; Joe et al., 2014; Liu et al., 2010; Lundquist et al., 2010; Marjanovic et al., 2010; Talbot et al., 2012; Zhu, 2008b). Joe et al. (2014) coupled WRF-LES with the Eulerian chemical model (WRF-Chem) to apply real Large Eddy nesting to multiple pollution sources modelling over a densely populated area of Oakland. The 250-m grid concentration outputs allow to highlight the need for explicit LES turbulent mixing instead of parameterized ensemble-mean turbulence to predict high exposure areas. The discrete grid of Eulerian models like WRF-Chem generates numerical diffusion errors (Brioude et al., 2013). Therefore in case of emissions from point sources, near-source concentrations are better represented by Lagrangian models which are independent from computational grid. Unlike Eulerian models, Lagrangian models have small computational costs. FLEXPART-WRF (Brioude et al., 2013), associating the Lagrangian Particle Dispersion Model FLEXPART (Stohl et al., 2005) and the regional meteorological model WRF, has been applied and validated for mid-range and long-range transport cases (de Foy et al., 2009; Angevine et al., 2013; Sandeepan et al., 2013; Heo et al., 2015; Madalaa et al., 2015). However, FLEXPART-WRF model has not been tested for very short-range transport and microscale resolution grids.

The main goal of the present work is to analyze the need for microscale nesting to prevent atmospheric pollution risks over a complex terrain. The case of the densely populated area of a small mountainous island, the Guadeloupe archipelago, is examined. This study showing the first evaluation of the FLEXPART-WRF model sensitivity at subkilometer resolutions has also of significant interest to near-source air quality research.

During a real case meteorological situation of weak trade winds, the transport and dispersion of nitrogen oxides (NO_x) emitted by the main power plant of Guadeloupe, is analyzed for three resolutions. Model outputs are evaluated with data recorded by two air quality stations. In the focused area, the main sources contributing to NO_x are the main power plant and vehicles on the primary road network. In order to identify the contribution of power plant and road traffic, inverse-modelling plumes of recorded NO_x peaks are also examined.

2. Methods

2.1. Description of the site

The Guadeloupe archipelago is located in the middle of the Lesser Antilles arc at 16.22° N and 61.55° W (Fig. 1). This archipelago includes two main islands: Basse-Terre, a mountainous island with a maximum elevation height of 1467 m and Grande-Terre, a low topography island with a maximum elevation height of 135 m. As written by Cécé et al. (2014), the special feature of Guadeloupe is the combination of two types of small island: the mechanical convective island of Basse-Terre ($Fr < 1$ and width ≤ 50 km) and the thermal convective island of Grande-Terre ($Fr \geq 1$ and width ≤ 50 km). Half of the total population, 200,000 people, live in the area located in the middle of the archipelago (16.20° N, 61.64° W; 16.28° N, 61.5° N) (Fig. 1). The low topography of this coastal region forming a basin between the two main islands (Fig. 1b) could generate calm winds and specific airflows in the atmospheric boundary layer. It is important to predict surface wind fields in this urban area which includes the main anthropogenic sources of atmospheric pollution: the main diesel power plant PWP (red circle, Fig. 1c) and the primary road network PRN (magenta lines, Fig. 1c). Observational data from the surface weather station WS2 (Fig. 1b) indicate that in this region of interest, under weak trade winds (≤ 5 m s^{-1}), a cold surface layer decreases the local wind speeds to null values during the night (Brévignon, 2003).

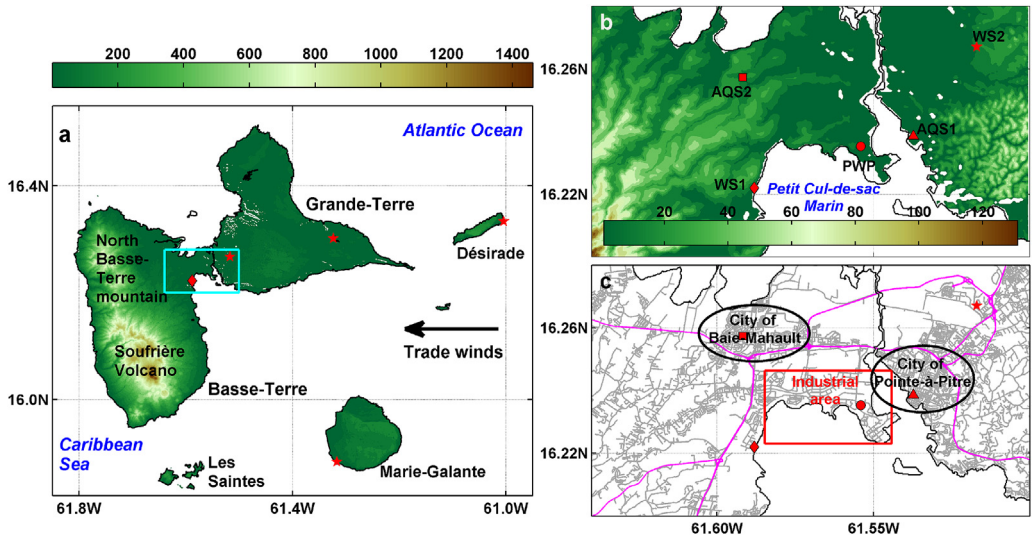

Fig. 1. Map of the Guadeloupe archipelago, including the 50-m resolution terrain height (m) and locations of four 1-h recording weather stations (red stars), one 1-Hz recording weather station (red diamond), two 15-min recording air quality stations; (a) The cyan rectangle corresponding to the most densely populated area zoomed in (b) and (c), including locations of two 15-min recording air quality stations and main power plant of the archipelago, respectively: AQS1 (red triangle), AQS2 (red square) and PWP (red circle); (c) indicating locations of the primary road network PRN (magenta lines) and the secondary one (grey lines). (For interpretation of the references to color in this figure legend, the reader is referred to the web version of this article.)

Under the same synoptic wind regime, at the weather station WS1 (Fig. 1b), D'Alexis et al. (2011) observed occurences of a reversed westerly nocturnal flow linked with sudden fall of 2-m air temperature. The coastal location of the observational point suggested that this westerly cold flow pushing the easterly trade winds offshore may be induced by the nocturnal land–sea thermal contrast as a land-breeze. Plocoste et al. (2014) field campaign showed that a similar westerly nocturnal flow appeared on the leeward coast of Grande-Terre, in Pointe-à-Pitre city (Fig. 1c). This circulation would transport VOCs from a landfill to residential areas. Plocoste et al. (2014) defined this nocturnal flow as a thermal breeze probably generated by an urban heat island. To identify the origin of this nocturnal flow observed on both sides of the urban area, Cécé et al. (2014) used the regional meteorological model WRF at spatial resolution of 1 km and temporal resolution of 1 h over the Guadeloupe archipelago. For three real cases of weather type linked with trade wind strength, strong ($\approx$12 m s^{-1}), medium ($\approx$6 m s^{-1}) and weak ($\approx$3 m s^{-1}), hourly 1-km output fields show good agreement with observational data from 5 surface weather stations and upper air soundings. These simulated data fields allowed to compensate for the lack of observational data over the Guadeloupe archipelago. Under weak trade winds, during the day, the convection is enhanced by the land–sea thermal contrast and the marine air-flow converges over lands. During the night, under weak trade winds, the model shows a good ability to reproduce the observed westerly flow. According to Cécé et al. (2014), this is a downslope wind initiated on the cold windward slopes of the Soufrière volcano. This flow extents downstream on the windward coast of Basse-Terre, then reaches the agglomeration area as far as Pointe-à-Pitre city. This kind of local circulations occurring over industrial plumes and the primary road network may enhance the risk for the health of the population. The small size of the region of interest (15.6 km $\times$ 8.9 km) and the small distance between potential industrial sources and residential areas located at less than 2 km suggest that the temporal resolution of 1 h and the spatial resolution of 1 km, respectively used in the Cécé et al. (2014) study should be decreased.

2.2. Simulation dates

The D'Alexis et al. (2011) observational study based on measurements of the 1-Hz recording station WS1 (red circle, Fig. 1b) allowed to record the only 10-min surface meteorological data in the region of interest. To validate the sub-hour WRF data sets of the present study, the simulation dates have been selected from the D'Alexis et al. (2011) field campaign period corresponding to the year 2007. The NO_x concentrations recorded during this year at AQS1 (i.e., the air quality station closest to the industrial area, Fig. 1c) indicate that the month of December testifies to the major pollution events (Fig. 2a1 and b1). During this dry season month, the largest hourly averaged concentration is observed between 0700 LT and 0800 LT, this period corresponding to the transition between nocturnal and diurnal wind regimes (Fig. 2a2 and b2). In December 2007, 40% of the 10-min wind speeds recorded at WS1 (i.e., the weather station closest to the industrial area, Fig. 1c) are lower than 3 m s^{-1} and 27% of the 10-min wind directions are westerly (Fig. 3). The study of three days of high NO_x concentrations and two days of weak pollution shows that NO_x peaks recorded in December at AQS1 are linked with weak winds and nocturnal westerly flows (Fig. 4).

Cécé et al. (2014) hourly 1-km numerical results allowed to analyze the onset and development of a nocturnal westerly downslope flow occurring during the weak trade winds period: 0600 UTC 3 December–0600 UTC 5 December 2007 (with UTC corresponding to LT + 4). In order to evaluate the contribution of sub-hour 1-km simulations and microscale simulations to this previous analysis, the same dates are examined with a time period reduced to 24 h: 1200 LT 3 December–1200 LT 4 December 2007. The hourly averaged NO_x concentrations (green triangles, Fig. 2a2) and the maximum values (red circles, Fig. 2b2) recorded at AQS1 during this period show that the selected days faithfully represent a typical case of severe pollution in the city of Pointe-à-Pitre. The clear sky and the small 24-h accumulated amount of rain (0.4 mm recorded by WS2) during this meteorological situation suggest that wet deposition removal processes of NO_x would be inhibited.

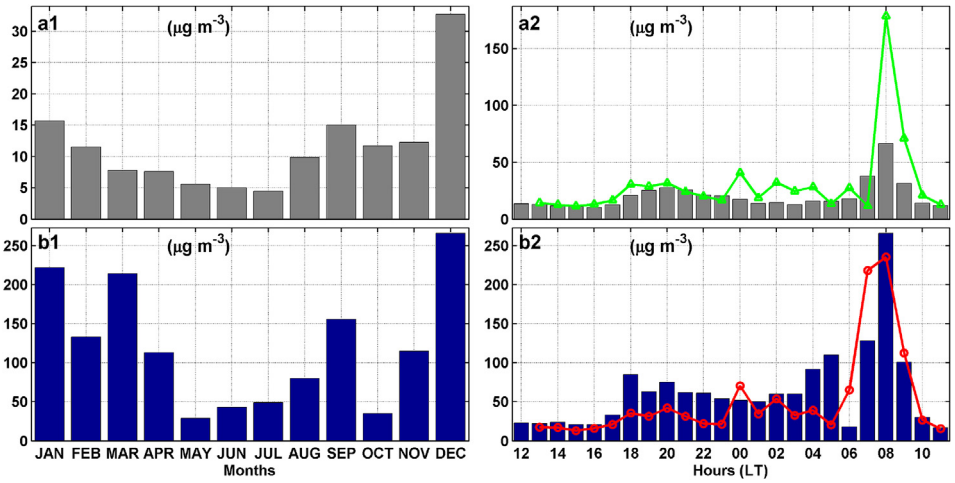

Fig. 2. NO_x concentrations ($\mu g\ m^{-3}$) recorded at AQS1 (i.e., the air quality station closest to the industrial area) in 2007: (a1) month means, (b1) month peaks, (a2) mean hourly values during December and (b2) maximum hourly values during December; with the hourly averaged concentrations (green triangles) and the maximum concentrations (red circles) recorded during the studied 24-h period. (For interpretation of the references to color in this figure legend, the reader is referred to the web version of this article.)

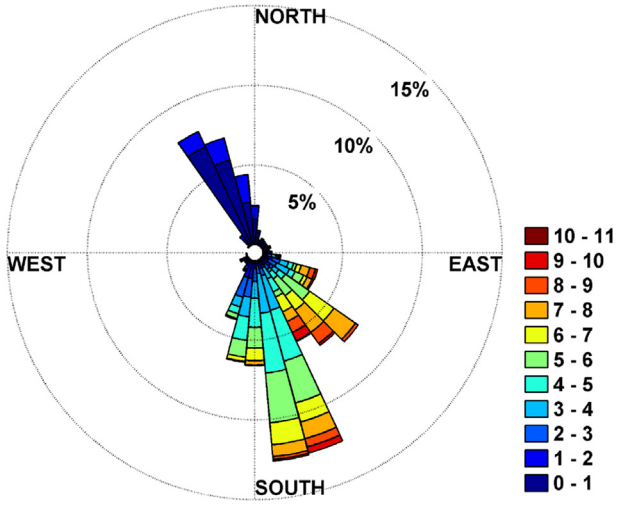

Fig. 3. Wind rose of the 10-m wind speed (m s^{-1}) and direction (°N) data recorded every 10 min at WS1 (i.e., the weather station closest to the industrial area) during the month of December 2007.

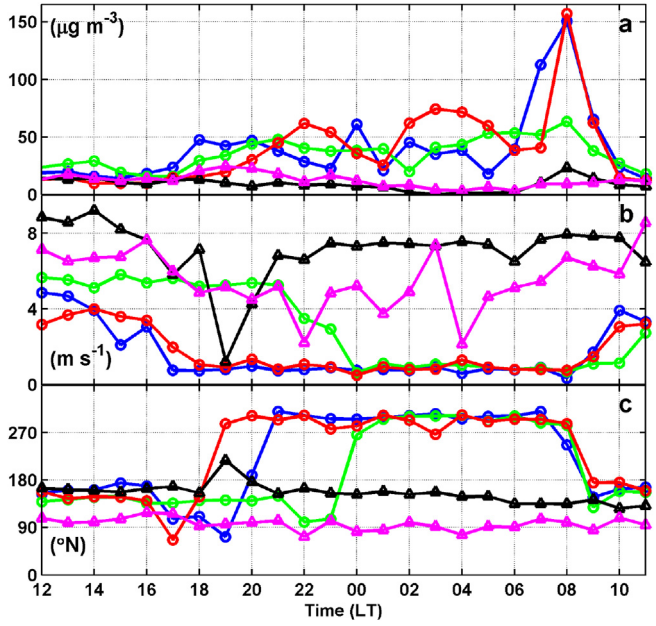

Fig. 4. Hourly surface data observed during five days, 3 December 2007 (blue circles), 10 December 2007 (black triangles), 14 December 2007 (magenta triangles), 22 December 2007 (green circles) and 23 December 2007 (red circles): (a) NO_x concentrations ($\mu g\ m^{-3}$) recorded at AQS1, (b) the 10-m wind speed (m s^{-1}) recorded at WS1 and (c) the 10-m wind direction (°N) recorded at WS1. (For interpretation of the references to color in this figure legend, the reader is referred to the web version of this article.)

2.3. Real nested Large-Eddy simulation setup

Three resolution grid outputs are compared in the present study: 1 km, 333 m and 111 m. The 333 m grid size corresponds to the usually called "turbulence grey zone" or "terra incognita" where the turbulent motions could not be entirely parameterized by an ensemble-mean scheme or mainly resolved by an LES scheme (Honnert et al., 2011; Wyngaard, 2004). In order to determine if at this resolution, the 1D ensemble-mean scheme, associated with lower computational costs, could well predict pollutant concentrations, an additional simulation is made in the 333 m domain with the 1D ensemble-mean scheme. This additional simulation also allows to dissociate grid resolution effects from the turbulence scheme ones. The Numerical Weather Predicted model WRF ARW V3.4.1 (Skamarock et al., 2008) is employed to produce 1-km, 333-m and 111-m resolution meteorological fields with a history interval of 10 min. These meteorological outputs are needed to force the Lagrangian Particle Dispersion Model FLEXPART-WRF (Brioude et al., 2013). The real nesting from largescale to microscale resolutions is performed with six domains D1, D2, D3, D4, D5 and D6 respectively associated to grid spacings 27 km, 9 km, 3 km, 1 km, 333 m and 111 m (Fig. 5). As described by Cécé et al. (2014), the outermost domain (D1) covers 80 × 80 grid cells in the central Atlantic area from South America to the Dominican Republic (Fig. 5a). The innermost domain (D6) covers 168 × 99 grid cells in the densely populated area of Guadeloupe (Fig. 5b). In the three finest-grid domains (D4, D5, D6), the topography of the Guadeloupe archipelago (domains D4, D5 and D6) was interpolated from the Institut Géographique National (IGN) 50-m topographic map and its land-use was interpolated from the 25-m Corine Land Cover map (CLC2006, EEA (2007)) pre-converted to 24 USGS land-

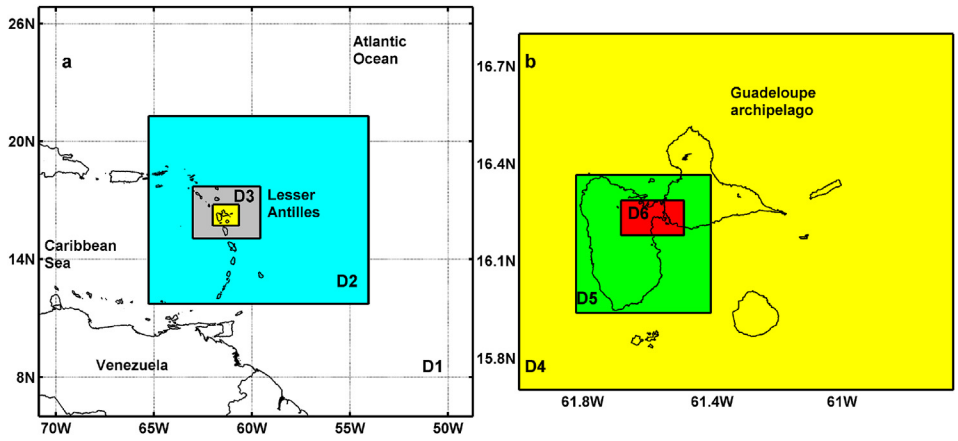

Fig. 5. WRF domains IOA: (a) two-way mesoscale nesting including domain D1 (white, 27 km of resolution), domain D2 (cyan, 9 km of resolution), domain D3 (grey, 3 km of resolution), domain D4 (yellow, 1 km of resolution); (b) one-way microscale nesting including domain D4, domain D5 (green, 333 m of resolution) and domain D6 (red, 111 m of resolution). (For interpretation of the references to color in this figure legend, the reader is referred to the web version of this article.)

use categories (Anderson et al., 1976; Pineda et al., 2004). All domains have 70 unequally spaced half vertical eta-levels with the lowest half level at 13 m AGL. The first 3000 m are set with 43 vertical levels. The model top is set at 100 hPa pressure level (i.e. the tropopause). To prevent reflections of gravity-wave energy at the top boundary, Rayleigh damping on vertical velocity option is turned on with a damping layer depth of 5 km. Most of Cécé et al. (2014) physics parameterizations are applied. In all domains, the surface layer is parameterized with Monin-Obukhov similarity. The WRF single-moment 6-class microphysics scheme Hong and Lim (2006) is selected. However, observational data showed that the cloud cover was negligible during the studied period in the focused area: a clear sky linked with a small 24-h accumulated amount of rain (0.4 mm recorded by WS2). The radiation is computed by the Rapid Radiative Transfer Model (RRTM) longwave scheme (Mlawer et al., 1997) and the Dudhia shortwave scheme (Dudhia, 1989). To well simulate radiation processes over the complex topography of Guadeloupe, the slope effects and the neighboring-point shadow effects are parameterized for domains D3, D4, D5 and D6. The Noah land surface model (Chen and Dudhia, 2001) is selected with the SST skin option which simulates the sea skin temperature diurnal cycle. In all domains the convection is explicitly resolved except for domain D1 where the Kain-Fritsch scheme Kain (2004) parameterizes the convection. In mesoscale domains (D1, D2, D3 and D4), the PBL is modelled by the ensemble-mean non-local-K YSU scheme Hong et al. (2006) which is associated with the horizontal first-order Smagorinsky closure. Comparative studies of WRF PBL schemes showed that YSU scheme was the best during convective boundary layer Shin and Hong (2011); Hu et al. (2010). However, under nocturnal stable conditions, the YSU scheme (WRF versions earlier than 3.4.1 version) had a tendency to inhibit vertical wind gradient (Hu et al., 2013). The decrease of nocturnal vertical mixing in the 3.4.1 version of WRF (used here), allows to improve simulation of wind speed in the lower layers during the night (Hu et al., 2013). This PBL scheme also showed good performances for WRF-LES coupling in cases of real nested microscale simulations (Joe et al., 2014; Talbot et al., 2012; Zhu, 2008a, b). In microscale domains (D5 and D6), the PBL is resolved explicitly by 3D Large Eddy Simulation equations (Moeng et al., 2007) with the 1.5 order TKE closure (Lilly, 1967). The WRF-333m-LES and WRF-111m-LES simulations have a time step of 0.3 s and 0.1 s, respectively. An additional 333-m simulation is made running the microscale domain D5 with the PBL YSU scheme (WRF-333m-YSU).

The real nested Large-eddy simulations are performed in two steps. First, a two-way four-level downscaling (D1, D2, D3 and D4) allows to obtain 1-km meteorological fields over the Guadeloupe archipelago with a history interval of 10 min (WRF-1km-YSU). In this mesoscale nesting, domain D1 is 6-hourly initialized with meteorological data from the 110 km NCEP FNL operational model global tropospheric analyses (continuing from July 1999, available online at http://rda.ucar.edu/datasets/ds083.2/). Then, a one-way two-level downscaling (D5 and D6) is used to obtain 333-m and 111-m meterorological fields over the focused urban area with a history interval of 10 min (i.e., WRF-333m-LES and WRF-111m-LES). In order to determine how the resolution affects the model performance, the one-way downscaling excluding nested feedback impacts should be preferably used. Lateral boundary conditions of domain D5 in WRF-333m-YSU and WRF-333m-LES are defined every 10 min by the 1-km domain D4 outputs which are pre-interpolated with a cubic-spline method.

This setup is used to simulate a time period of 60 h (from 1800 UTC 2 December to 0600 UTC 5 December 2007). The first 12-h results are not examined, this period corresponds to the typical spinup time period (Hu et al., 2010).

2.4. Lagrangian Particle Dispersion Model setup

The main goal of the present numerical study is to analyze effects of microscale resolutions on the dispersion of NO_x emitted by anthropogenic sources in a densely populated area of Guadeloupe. The main sources of NO_x in this region are the most important diesel power plant PWP and vehicles on the primary road network PRN. The Lagrangian Particle Dispersion Model FLEXPART-WRF (Brioude et al., 2013; Stohl et al., 2005) is used to simulate the forward and backward dispersions of NO_x in domains D4, D5 and D6: FLEXPART-1km-YSU, FLEXPART-333m-YSU, FLEXPART-333m-LES and FLEXPART-111m-LES. The respective WRF grids (i.e., WRF-1km-YSU, WRF-333m-YSU, WRF-333m-LES and WRF-111m-LES) are used for single pollution simulations corresponding to each domain. The vertical grid includes 38 terrain-following levels with the first level at 10 m AGL and the model top at 3000 m AGL. The WRF outputs reinitialize FLEXPART-WRF model every 10 min. The main meteorological input variables include: mass-weighted time-averaged wind fields, friction velocity, heat sensible flux and PBL height. The PBL turbulence is parameterized by the Hanna scheme (Hanna, 1982) which computes turbulent profiles depending on stability conditions of the PBL.

The dispersion of NO_x emitted by the power plant PWP is

simulated in domains D4, D5 and D6, during a period of 24 h: 1200 LT 3 December–1200 LT 4 December 2007. Like concentrations measured by the air quality stations AQS1 and AQS2, simulated concentrations are averaged and saved every 15 min. The PWP plume is represented by a column of 30 × 30 × 340 m centered at 61.5515° W and 16.2280° N (Fig. 1c). The plume base corresponds with smokestack height of 60 m AGL. Following PWP plume observational pictures, the plume top is set at 400 m AGL. According to the Pollutant Emissions French Register, the power plant PWP released 9.790 kilotons of NO_x (equivalent NO_2) in 2007. On the basis of this amount, the NO_x total mass emitted by PWP during 24 h is set to 26.820 tons with a constant emission rate as no hourly profile information is available. This assumption might increase the uncertainties in the calculated NO_x concentrations. In the model, the concentrations are calculated on the basis of the number of trajectories located within each grid cell and their mass fraction. The larger the number of released particles is, the better the particle mass fraction statistics for each grid cell are represented. Hence, for a given resolution grid, an optimal number of trajectories to run in the model needs to be estimated. In order to determine this number corresponding to result stability, several simulation tests have been made with a number of particles released every 15 min ranging from 5000 to 60,000 particles. These tests have shown that the result stability is reached for 1-km grid, 333-m grid and 111-m grid, with the respective number of particles emitted every 15 min during the 24-h period: 20,000, 30,000 and 50,000.

Backward simulations allow to analyze retroplume and sources of NO_x peaks recorded at AQS1 and AQS2. In the region of interest, the power plant PWP and the primary road network PRN are the potential sources of this pollution (Fig. 1c). Because of the short distances between these sources and the air quality stations (e.g., the distance from PWP to AQS1 is equal to 1.75 km and the distance from PRN to AQS2 is equal to 650 m), the simulation period is set to 24 h from peak times with a history interval of 5 min. Source sensitivity fields, related to the residence time of particles in grid cells, are obtained for the three resolution grids. The residence time is linked with the number of particles flowing in each grid cell. The smaller the grid cell is, the shorter the residence time of a particle in this cell is. In order to determine the number of particles to release, several simulation tests have been made with respectively 25,000, 50,000 and 100,000 released particles. These tests have shown that to keep residence time values consistent in the 111-m grid, it is necessary to use 100,000 particles. This number of released particles is also used for the two larger grids. The particles are released at observed peak times in each domain. The air quality stations are represented by boxes of 20 × 20 × 10 m at 10 m AGL. These boxes are centered on AQS1 location (16.2385° N, 61.5377° W) and AQS2 location (16.2573° N, 61.5917° W).

3. Results and discussion

3.1. Effects of the resolution on simulated meteorological fields

3.1.1. Comparison of terrain data for the three resolutions

The relatively flat topography of the focused area includes the highest terrain elevation of 131 m on the windward slopes of Basse-Terre island (Fig. 6d). The low topography around the source PWP and the station AQS1 suggests weak shear inhibiting turbulent motions and particle dispersion. The 1-km interpolated topography smoothes this basin area between Basse-Terre island and Grande-Terre island (Fig. 6a). While the 333-m interpolated topography renders the main relief patterns, the 111-m grid defines most details of the original 25-m topography (Fig. 6).

The main land-use categories in the region of interest include: marine surfaces, urban and built-up land and crops/wood mozaic (Fig. 7d). These land-use categories determine albedo and roughness length values which are critical parameters affecting skin surface temperature and friction velocities. When the albedo decreases, the skin surface temperature has greater values which may induce turbulent rising motions. Great roughness length values generate higher friction velocities and lower surface horizontal wind speeds. The thermal land-sea contrast is a significant forcing inducing local circulations, like diurnal–nocturnal convergence–divergence of surface winds over land (Cécé et al., 2014). The 1-km resolution grid represents poorly the 25-m resolution coastline with PWP and AQS1 located in marine areas (Fig. 7a). The increase in resolution to 333-m spacing grid allows to better represent the industrial area including PWP while AQS1 is still located in the sea (Fig. 7b). The 111-m resolution landuse map defines most details of the 25-m resolution coastline and shows realistic landuse categories for PWP and all observational surface stations (Fig. 7c).

3.1.2. Evaluation of simulated meteorological fields

Four surface meteorological variables (2-m temperature, 2-m water vapor mixing ratio, 10-m wind speed and direction) are evaluated with observational data recorded at WS1 and WS2 (Figs. 1b and 8). The 24 h period of the particle dispersion modelling (1200 LT 3 December–1200 LT 4 December 2007) is studied. While the 1-h recorded data from WS2 allow an approximated evaluation of the 10-min model outputs (Fig. 8a1–a4), the 1-Hz recorded data from WS1 allow an evaluation at a specific history interval of 10 min (Fig. 8b1–b4). As described by Cécé et al. (2014) for wind speed, WS1 and WS2 have respectively an accuracy of 2% (with a resolution of 0.01 m s^{-1}) and 1 m s^{-1}. Thus instead of WS1, WS2 is unable to record wind speed values lower than 1 m s^{-1} which are common during the night. This induces missing values for 10-m wind speed and direction observed at WS2 urban station (Fig. 8a3 and a4).

The 2-m air temperature and the 2-m water vapor mixing ratio are the worst simulated variables at WS2 location (Fig. 8a1–a4). For the four simulations (i.e., WRF-1km-YSU, WRF-333m-YSU, WRF-333m-LES and WRF-111m-LES), the simulated temperature is overestimated during the night with a maximum bias of 4 °C at 0800 LT. On the contrary, the simulated water vapor mixing ratio is globally underestimated with a bias of 2.5 g kg^{-1}). For the three resolutions, the WS2 location corresponds to the urban land-use category which is parameterized by large heat storage and low evaporation whereas WS2 sensors are located over airport grassland. Wind speed and direction seem to be well simulated at WS2 (Fig. 8a3 and a4). During the night, simulation outputs show occurrences of westerly flows. Unfortunately, these nocturnal circulations linked with wind speed lower than 1 m s^{-1} cannot be recorded by WS2 wind sensor. For the three resolutions, the location of WS1 coastal station corresponds to the mangrove land. At this land-sea interface point, the four variables seem better simulated in the 111-m grid (red line, Fig. 8b1–b4). For the 2-m temperature, WRF-1km-YSU, WRF-333m-YSU and WRF-333m-LES outputs show similar values with large underestimations of the nocturnal radiative cooling (Fig. 8b1). The maximum difference between observational data and these outputs reaches 3.7 °C at 0530 LT. For all simulations, the model inhibits the diurnal variation of air temperature and overestimates the water vapor mixing ratio (Fig. 8b1 and b2). The wind speed is the worst simulated variable with a model steady overestimation of 2 m s^{-1} during the night (Fig. 8b3). These errors would be generated by model roughness length smaller than reality. These overestimated wind speeds could induce underestimated concentrations in the particle dispersion model. For the three resolutions, the model well reproduces the westerly downslope flow occurring on the windward slopes of

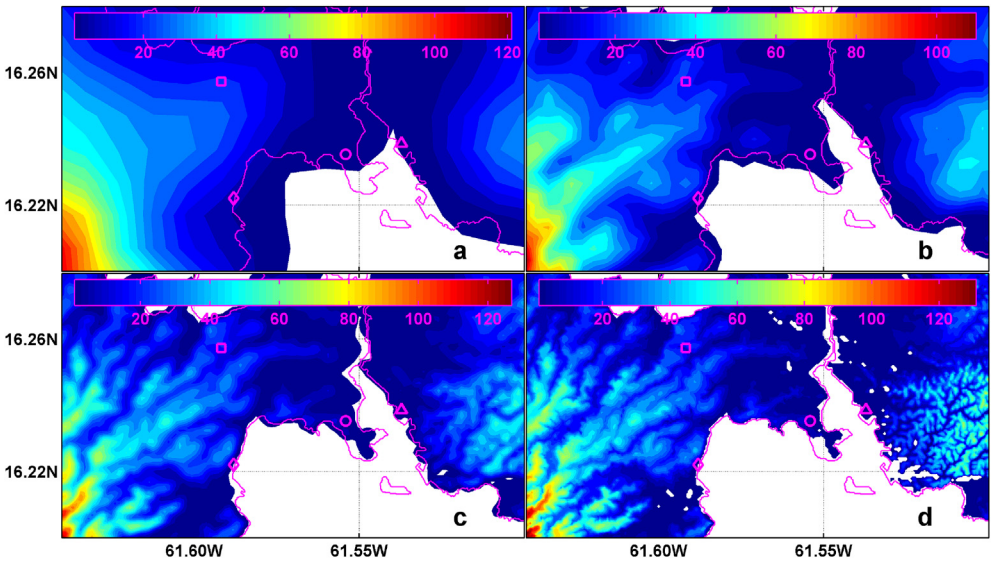

Fig. 6. Maps of topography (m): (a) 1-km resolution grid, (b) 333-m resolution grid, (c) 111-m resolution grid, (d) original 50-m resolution grid with diamond, star, triangle, square and circle corresponding respectively to weather station WS1, weather station WS2, air quality station AQS1, air quality station AQS2 and power plant PWP; magenta line indicating the 25-m resolution coastline. (For interpretation of the references to color in this figure legend, the reader is referred to the web version of this article.)

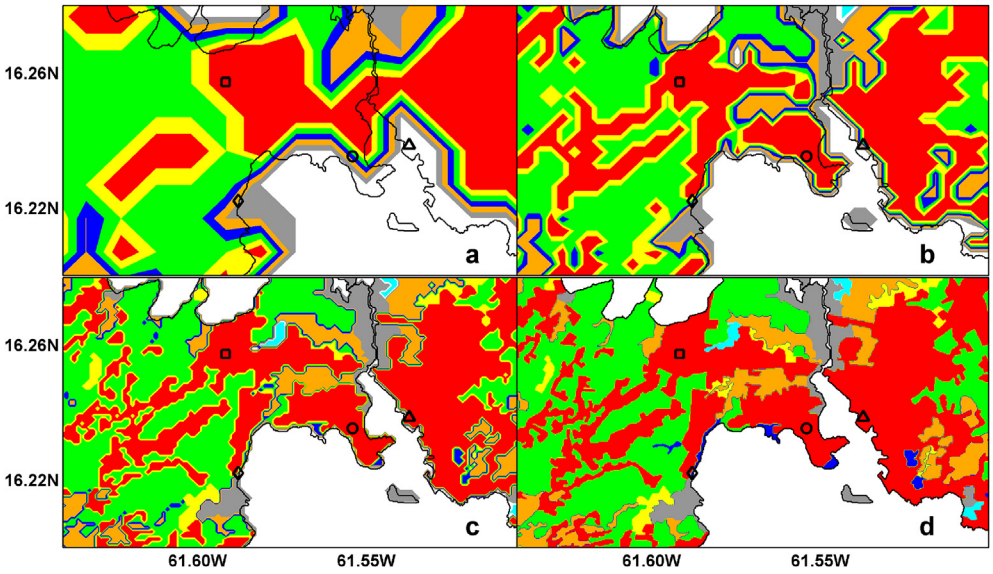

Fig. 7. Map of land-use categories in the focused area with water bodies (white), urban and built-up land (red), mixed forest and mangrove (grey), dryland cropland and pasture (yellow), crops/wood mozaic (green), deciduous broadleaf forest (orange), mix shrubland/grassland (blue), herbaceous wetlands (cyan); diamond, star, triangle, square and circle corresponding respectively to weather station WS1, weather station WS2, air quality station AQS1, air quality station AQS2 and power plant PWP; black line indicating the 25-m resolution coastline; (a) 1-km resolution grid, (b) 333-m resolution grid, (c) 111-m resolution grid, (d) original 25-m resolution grid. (For interpretation of the references to color in this figure legend, the reader is referred to the web version of this article.)

Basse-Terre island (Fig. 8b4). During this established nocturnal circulation, non-real west-southwest wind directions linked with increased wind speed are simulated. These biases may be induced by errors in parameterization of friction velocity at this coastal mangrove area.

Overall, for the two locations and the four meteorological variables, timeseries shows slight differences between the four simulations. In order to estimate the effects of microscale dowscalling on model performance, a statistical evaluation is needed. The error estimators (MBE, MAE, IOA) are computed with observational data recorded at WS1 station (Table 1) and at AQS2 station (Table 2). These statistical error estimators are described in the appendix. The index of agreement IOA is based on variations of the MAE (Willmott et al., 2012). As written by Cécé et al. (2014), the model performance is considered as bad, good, and very good when IOA values are respectively: negative, between 0 and 0.5 and above 0.5.

At WS1 location, for any grids and any variables (Table 1), the model shows good scores (i.e., IOA values above 0) and generally the rise of resolution improves the model sensitivity. For any case, the use of LES scheme instead of the YSU scheme at 333 m resolution, slightly enhances the model prediction. The wind speed is the worst simulated variable. This may be explained by the nocturnal model overestimations previously described and by large observed variations of wind speed (i.e., mean and standard

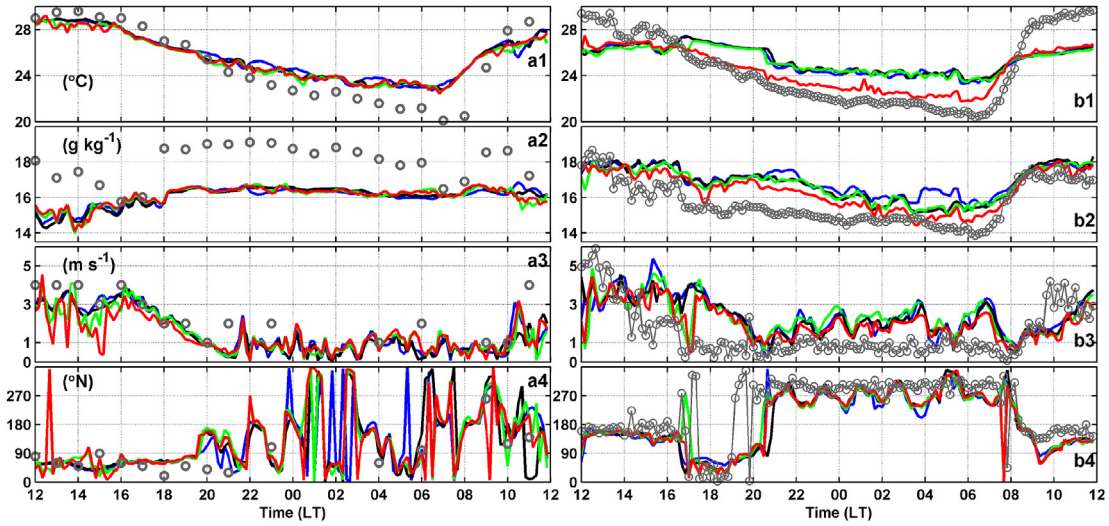

Fig. 8. Comparison between WRF-1km-YSU (blue line), WRF-333m-YSU (black line), WRF-333m-LES (green line), WRF-111m-LES (red line) and observational data (grey circles) for four variables: (a1,b1) 2-m air temperature (°C), (a2,b2) 2-m water vapor mixing ratio (g kg^{-1}), (a3,b3) 10-m wind speed (m s^{-1}), (a4,b4) 10-m wind direction (°N) at two locations, (a1–a4) 1-h recording weather station WS2 and (b1–b4) 1-Hz recording weather station WS1. (For interpretation of the references to color in this figure legend, the reader is referred to the web version of this article.)

Table 1
Surface WRF data evaluation at WS1 location during the period of 24 h (144 points).

	Air temperature (°C)	Vapor mixing ratio (g kg^{-1})	Wind speed (m s^{-1})	Wind direction (°N)
Obs mean	24.56	15.68	1.50	272.55
Obs std dev	3.09	1.19	1.33	40.21
WRF-1km-YSU				
MBE	0.81	1.29	0.93	−15.58
MAE	2.24	1.34	1.39	44.78
IOA	0.60	0.35	0.33	0.66
WRF-333m-YSU				
MBE	0.85	1.11	0.83	−21.12
MAE	2.35	1.16	1.29	41.68
IOA	0.58	0.43	0.37	0.68
WRF-333m-LES				
MBE	0.74	1.04	0.81	−16.72
MAE	2.32	1.14	1.27	41.22
IOA	0.59	0.44	0.38	0.69
WRF-111m-LES				
MBE	−0.03	0.70	0.57	−17.14
MAE	1.29	0.81	1.13	39.06
IOA	0.77	0.61	0.45	0.70

Table 2
Surface WRF data evaluation at AQS2 location during the period of 24 h with a time step of 15 min (40 points available).

	Wind speed (m s^{-1})	Wind direction (°N)
Obs mean	1.33	328.87
Obs std dev	0.49	35.93
WRF-1km-YSU		
MBE	0.05	−32.64
MAE	0.68	70.11
IOA	0.16	0.76
WRF-333m-YSU		
MBE	0.47	−6.49
MAE	0.78	44.90
IOA	0.01	0.85
WRF-333m-LES		
MBE	0.43	−1.75
MAE	0.67	44.44
IOA	0.16	0.86
WRF-111m-LES		
MBE	0.38	0.52
MAE	0.67	40.79
IOA	0.16	0.86

deviation have the same order of magnitude). With very good scores for the four simulations (i.e., IOA values above 0.5), the wind direction and the 2-m air temperature are the best simulated variables. Contrary to the dynamical variables, for 2-m temperature and vapor mixing ratio, the nesting from the 333-m grid to the 111-m grid allows to significantly improve model–observations agreement. This would be induced by the buoyant turbulent motions which are better resolved at the LES scale of 111 m than at the "turbulence grey" scale of 333 m.

The 10-m wind speed and direction data recorded every 15 min at the air quality station AQS2 are used to evaluate the model at a second grid point (Table 2). During the 24-h studied period, due to the weak sensitivity of the AQS2 wind sensor (minimum wind speed recorded of 0.5 m s^{-1}), only 40 observational data are available. At this location, the wind direction is very well simulated with a significant improvement with the nesting to the 333-m resolution. For the wind speed, except the WRF-333m-YSU simulation which has the worst score, the models have the same good IOA value for all grids. Overall, in this urban area characterized by a

relative flat topography (Figs. 6 and 7), the grid resolution has a small impact on the predicted 10-m winds.

3.1.3. Expected accumulation areas

In FLEXPART-WRF, turbulent mixing is parameterized by the Hanna scheme which computes standard deviations of turbulent velocity fluctuations depending on Richardson number values (i.e., stability conditions of the ABL). The following Richardson number values: negative, null, between 0 and 0.2, and greater than or equal to 0.2, correspond respectively to stability regimes: unstable, neutral, mechanical turbulent and stable. During the day, convective turbulent motions in unstable ABL enhance the dispersion of particles whereas the nocturnal stable condition enhances their accumulation. In order to predict areas of particle accumulation–dispersion, the gradient Richardson number representing the ratio between the buoyant production and the shear production of turbulence is defined between 13 m AGL and 100 m AGL as:

$$\mathrm{Ri} = \frac{\frac{g}{T_v}\frac{\partial \theta v}{\partial z}}{\left(\frac{\partial U}{\partial z}\right)^2 + \left(\frac{\partial V}{\partial z}\right)^2}, \quad (1)$$

where g is the gravitational acceleration, T_v is the virtual temperature at 100 m AGL, θv is the virtual potential temperature, U and V are the horizontal wind components. This dimensionless ratio is averaged on a diurnal period (3 December 1200–1800 LT) and on a nocturnal period (3 December 2200 LT–4 December 0600 LT).

In diurnal and nocturnal conditions, the WRF-333m-LES and WRF-111m-LES domains show quite similar Richardson number patterns (Fig. 9). During the day, most parts of the focused area are under unstable dispersive conditions, rising motions would enhance the dispersion of emitted particles (Fig. 9a1–a4). The subkilometer resolution domains allow to predict a shear-driven dispersion area on the leeward side of Grande-Terre (Fig. 9a2–a4). During the night, there are significant biases for accumulation areas between the 1-km resolution domain and the microscale ones (Fig. 9b1–b4). While the WRF-1km-YSU output predicts these potential pollution areas on the west side of the urban areas, the three finer domains locate them on the east side including the industrial area (PWP source) and the city of Pointe-à-Pitre (AQS1 station). This suggests that compared to the subkilometer domains, the 1-km resolution domain would underestimate nocturnal concentrations of NO_x emitted by PWP and the induced health risk in this part of the domain. At 333-m resolution, the YSU turbulence scheme tends to predict smaller potential pollution areas than the 3D LES scheme.

3.2. Forward modelling of NO_x emitted by PWP

3.2.1. Diurnal and nocturnal dispersion of PWP NO_x

During the afternoon, the first 100-m levels and 5 h averaged horizontal wind fields are characterized by wind speeds lower than 4.5 m s^{-1} and a convergence area linked with sea breeze circulations (Fig. 10a1–a4). Compared to the LES domains, the 1 km- and 333m-YSU wind speeds are generally larger inhibiting the low wind area simulated on the leeward side of Grande-Terre. Around the PWP source, the YSU outputs show an east southeast mean wind direction whereas the LES output indicates a south southeast wind direction. The first 100-m levels and 5 h averaged diurnal NO_x concentrations are plotted for values between 25 and 200 $\mu g\ m^{-3}$ (Fig. 10b1–b4). The 1-km plume is confined in one grid at the left of PWP location with low maximum value of 59 $\mu g\ m^{-3}$. The FLEXPART-333m-LES and FLEXPART-111m-LES plume extends in the industrial area (2.5 km from PWP) with near-source concentrations exceeding the World Health Organization risk value of 200 $\mu g\ m^{-3}$. At the PWP, the maximum values of concentrations simulated in FLEXPART-333m-LES and FLEXPART-111m-LES domains, reach respectively 228 and 423 $\mu g\ m^{-3}$. The FLEXPART-333m-YSU plume extends in the same direction as the FLEXPART-333m-LES one. However, at this resolution, the YSU outputs associated with larger wind speeds produce near-source concentrations well lower than the risk value of 200 $\mu g\ m^{-3}$.

The nocturnal PWP plume is analyzed averaging wind speeds and NO_x concentrations values between 2200 LT and 0600 LT. The mean simulated nocturnal wind field seems to depend less on the three selected resolutions (Fig. 11a1–a4). For the four simulations, the westerly downslope wind initialized on the mountain windward slopes, extends to Grande-Terre island, flowing over the industrial area and PWP location. This particular flow converges with land-breeze circulations on the leeward coast of Grande-Terre island. The averaged NO_x concentrations are plotted for values between 25 and 400 $\mu g\ m^{-3}$ (Fig. 11b1–b4). As for the diurnal case, the simulated near-source concentrations increase with the resolution. Maximum values simulated in FLEXPART-1km-YSU, FLEXPART-333m-YSU, FLEXPART-333m-LES and FLEXPART-111m-LES are respectively: 191, 412, 460 and 957 $\mu g\ m^{-3}$. This rise in near-source concentration is linked with a lower volume of grid cells. Instead of these concentration peaks, the averaged FLEXPART-333m-YSU, FLEXPART-333m-LES and FLEXPART-111m-LES NO_x plumes are quite similar. For the four simulations, the plume (25 and 100 $\mu g\ m^{-3}$) extends to the northside of the urban area, taking apparently a direction opposed to the mean wind patterns. This part of the plume located in a calm wind area, corresponds to the deposition of NO_x emitted above 250 m AGL (i.e. top of the westerly

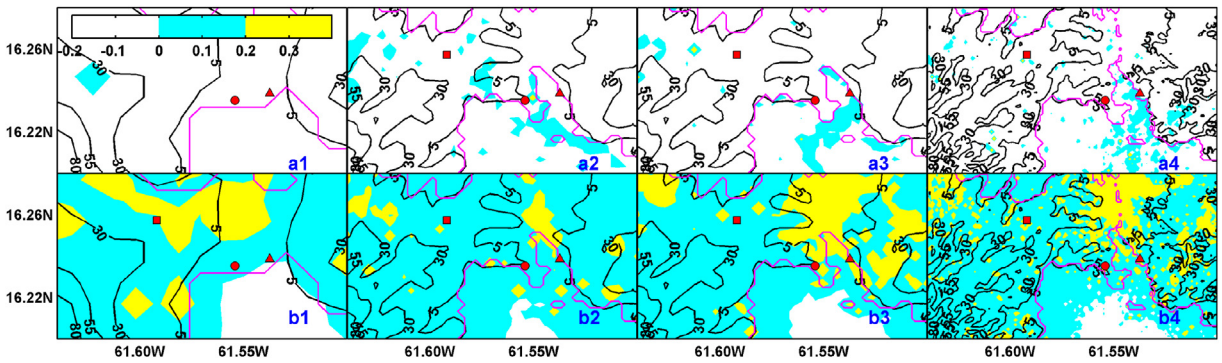

Fig. 9. Averaged diurnal (a1–a3) and nocturnal (b1–b3) gradient Richardson number for the four simulations including terrain elevation (black contours): (a1,b1) WRF-1km-YSU, (a2,b2) WRF-333m-YSU, (a3,b3) WRF-333m-LES and (a4,b4) WRF-111m-LES with locations of AQS1, AQS2 and PWP, respectively red triangle, red square and red circle. (For interpretation of the references to color in this figure legend, the reader is referred to the web version of this article.)

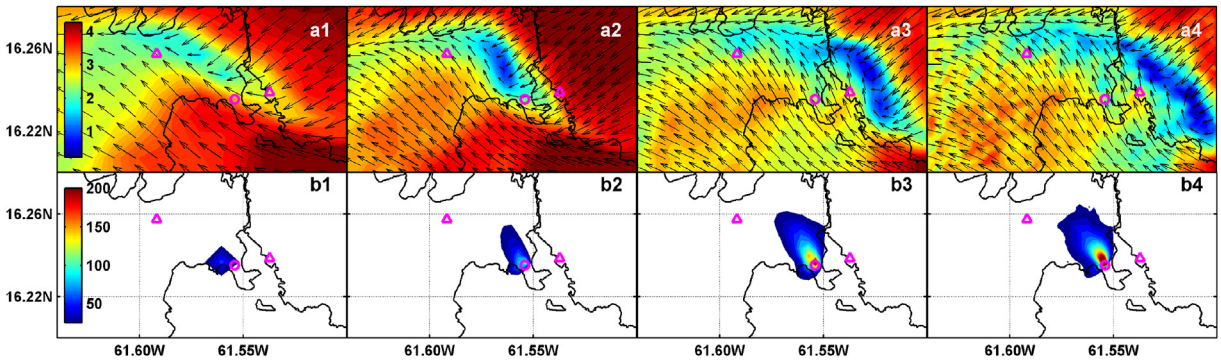

Fig. 10. Diurnal plume averaged on the first 100 m AGL and on the temporal period of 1200 LT to 1700 LT, (a1–a3) averaged horizontal wind speed (m s^{-1}), (b1–b3) averaged concentration (μg m^{-3}) for the four simulations: (a1,b1) FLEXPART-1km-YSU, (a2,b2) FLEXPART-333m-YSU, (a3,b3) FLEXPART-333m-LES and (a4,b4) FLEXPART-111m-LES with locations of AQS1 (magenta triangle), AQS2 (magenta square) and PWP (magenta circle). (For interpretation of the references to color in this figure legend, the reader is referred to the web version of this article.)

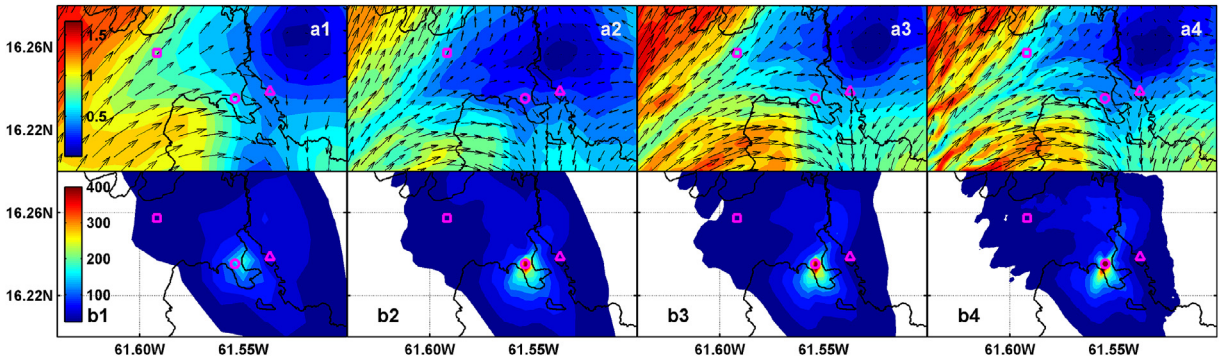

Fig. 11. Nocturnal plume averaged on the first 100 m AGL and on the temporal period of 2200 LT to 0600 LT, (a1–a3) averaged horizontal wind speed (m s^{-1}), (b1-b3) averaged concentration (μg m^{-3}) for the four simulations: (a1,b1) FLEXPART-1km-YSU, (a2,b2) FLEXPART-333m-YSU, (a3,b3) FLEXPART-333m-LES and (a4,b4) FLEXPART-111m-LES with locations of AQS1 (magenta triangle), AQS2 (magenta square) and PWP (magenta circle). (For interpretation of the references to color in this figure legend, the reader is referred to the web version of this article.)

downslope flow).

3.2.2. *Evaluation of NO_x simulated concentrations*

For the 24 h period, surface NO_x simulated concentrations are compared with the 15-min recorded data from AQS1 and AQS2 (Fig. 12). The two main sources of NO_x are located less than 2 km from AQS1: the primary road network PRN and the PWP plant are located respectively at 1.6 km east and 1.7 km west of AQS1 (Fig. 1c). From midnight to 1000 LT, the westerly nocturnal flow transports PWP NO_x to AQS1 location (Fig. 12a1–a3). Globally, observational pollution peaks (0115, 0330 and 0715 LT) are reproduced for the four simulations with a tendency to overestimate concentrations. This current bias is probably induced by an input emitted total mass larger than reality. For the three resolutions, the most important peak of 236 $\mu g\ m^{-3}$, observed at 0715 LT, is the best simulated peak. The AQS1 station is located at the convergence area between the westerly downslope flow and the easterly land breeze flow. FLEXPART-1 km-YSU shows large overestimations between 0000 LT and 0400 LT. During this period, the 1-km output indicates a sustainable north-west direction whereas the subkilometer outputs simulate wind shear which seems more realistic.

The AQS2 station is located 4.7 km northwest of PWP and 650 m north of primary road network PRN. Model results show that diurnal and nocturnal circulations are able to transport NO_x from PWP to AQS2 (Fig. 12b1). While the two LES domains largely overestimate the peak observed at 2115 LT, the four simulations underestimate the main peak observed at 0730 LT. This underestimation occurring near PRN and at rush-hour traffic seems linked with vehicle NO_x emissions not taken into account in the model. This can also be explained by the overestimated WRF nocturnal surface wind speeds (observed at WS1 location). This peak observed and simulated at 0730 LT is linked with very low wind speed values induced during the transition between the nocturnal westerly flow and the diurnal easterly trade winds (Fig. 12b1–b3). At AQS2 location, the FLEXPART-333m-YSU concentrations follow variations of the FLEXPART-1km-YSU concentrations with a current overestimation of 20 $\mu g\ m^{-3}$. Overall, model outputs fit AQS1 observational concentrations better than AQS2 ones. As previously remarked in the WRF outputs validation, the surface wind fields simulated at AQS2 are quite similar for the three resolutions (Fig. 12b2 and b3). This suggests that at this inland urban location, microscale turbulent motions would have minor impacts on mean mesoscale diurnal and nocturnal circulations.

Concentrations simulated at the closest station from the source (AQS1) are evaluated with statistical tools (Table 3). The first 12 h are removed to avoid model concentration values equal to zero. For the four simulations, despite large observed variations (std dev of 53.5 $\mu g\ m^{-3}$), IOA values show good performance scores, including an improvement of model sensitivity with the increase in resolution. Indeed, with respective IOA values of 0.5, 0.5 and 0.6, the 333m-YSU, 333m-LES and 111m-LES outputs have very good agreement with the observations. As graphically remarked, the model tends globally to overestimate NO_x concentrations. While the nesting to subkilometer grids helps to reduce the MAE by

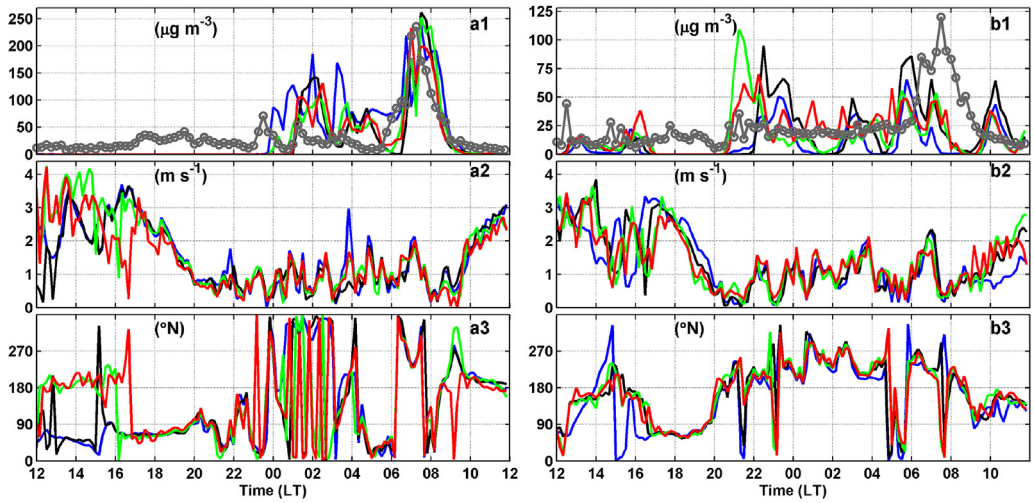

Fig. 12. Comparison between FLEXPART-1km-YSU (blue line), FLEXPART-333m-YSU (black line), FLEXPART-333m-LES (green line), FLEXPART-111m-LES (red line) and observational data (grey circles) at AQS1 location (a1–a4) ans AQS2 location (b1–b4), for three variables: (a1,b1) 10-m concentration (μg m^{-3}), (a2,b2) 10-m horizontal wind speed (m s^{-1}), (a3,b3) 10-m wind direction (°N). (For interpretation of the references to colour in this figure legend, the reader is referred to the web version of this article.)

Table 3
Simulated surface concentration (μg m^{-3}) evaluation at AQS1 location during the period from midnight to 1200 LT with a time step of 15 min (48 points).

	1km-YSU	333m-YSU	333m-LES	111m-LES
Obs mean	45.6	45.6	45.6	45.6
Obs std dev	53.5	53.5	53.5	53.5
MBE	32.9	5.5	11.9	8.0
MAE	49.1	40.0	36.9	32.4
IOA	0.4	0.5	0.5	0.6

9 μg m^{-3}, the use of the LES scheme in the 333-m grid domain allows to decrease it by 3 μg m^{-3}. LES domains better simulate turbulent motions governing the pollution dispersion in this convergence area between the westerly downslope flow and the easterly land-breeze.

3.3. Backward modelling of NO_x deposition peaks

In order to analyze the effects of resolution on source identification model, the two important peaks observed at AQS1 and AQS2 are simulated. These peaks are recorded by AQS1 at 2330 LT and 0715 LT with respective concentration values: 71 μg m^{-3} and 236 μg m^{-3}. For AQS2 these peaks occur at 2215 LT and 0730 LT with respective concentration values: 27 μg m^{-3} and 120 μg m^{-3}. Backward plume and source sensitivity are examined with 24-h averaged residence times. In order to examine the contributions of the primary road network PRN and the contributions of the power plant PWP, the residence time is vertically integrated in two layers, respectively 50–200 m AGL and 100–300 m AGL.

3.3.1. NO_x deposition peaks recorded by AQS1

During the first part of the night, before 2330 LT, the easterly land-breeze is predominant around AQS1 in the city of Pointe-à-Pitre (Fig. 12a3). The PWP plant can hardly be the source of the peak of NO_x. The previous forward simulations show concentration values equal to zero at this time (Fig. 12a1). For the four simulations, 24-h backward plumes suggest that the primary road network area located at 1.5 km from AQS1, may be the source of this deposition (Fig. 13). The increase in resolution allows to reproduce a more accurate plume from AQS1 to the source. Compared to FLEXPART-1km-YSU and FLEXPART-333m-LES, FLEXPART-333m-YSU and FLEXPART-111M-LES predict that NO_x would be emitted from a second, southern section of PRN (Fig. 13a2,b2,a4,b4). However, the FLEXPART-333m-YSU extends the potential source area easterly beyond the PRN location.

During the 24-h period, the most important peak was observed at AQS1 at the beginning of the morning at 0715 LT. At this time, the four forward outputs well simulate occurrence of this maximum deposition linking with a well established westerly flow (Fig. 12a1–a3). The back trajectories permit to examine the main trajectory of the particles emitted by the PWP plant (Fig. 14). To better define the plume from AQS1 to PWP plant, the residence time vertically integrated between 100 and 300 m AGL is analyzed (Fig. 14b1–b4). While FLEXPART-1km-YSU indicates a potential source area extending on the southside of the industrial area, the microscale models show a sharper plume flowing over the marine zone from PWP location.

3.3.2. NO_x deposition peaks recorded by AQS2

The pollution peak observed at 2215 LT at AQS2 was selected because at this time the four forward outputs simulate a simultaneous overestimated peak (Fig. 12b1). This fact would suggest contribution of PWP which is located at 4.7 km from AQS2. During this period, the westerly downslope flow is established around AQS2 but it is not extended to PWP location. Therefore NO_x emitted by the power plant may be transported to AQS2. For this peak, while FLEXPART-1km-YSU predicts the closer PRN section as the only source, FLEXPART-333m-YSU, FLEXPART-333m-LES and FLEXPART-111m-LES simulate PWP as the second source (Fig. 15). The microscale nesting allows to simulate the main trajectory of the industrial plume in the PWP sensitivity layer (Fig. 15b2–b4). In this vertical layer, in addition to the main back trajectory to PWP, the FLEXPART-333m-LES output shows a southern back trajectory. This secondary retroplume would be induced by particle recirculations during the transition between easterly diurnal flows and westerly nocturnal flows.

The time 0730 LT represents both the rush-hour traffic and the very low wind speed period induced by the transition from the westerly nocturnal flow to the easterly trade winds (Fig. 12b2 and b3). The four backward simulations predict the section of PRN which is located at 650 m from AQS2 (Fig. 16). The southern large area of high residence time values predicted by FLEXPART-WRF-111m in the PWP sensitivity layer, seems to be induced by the

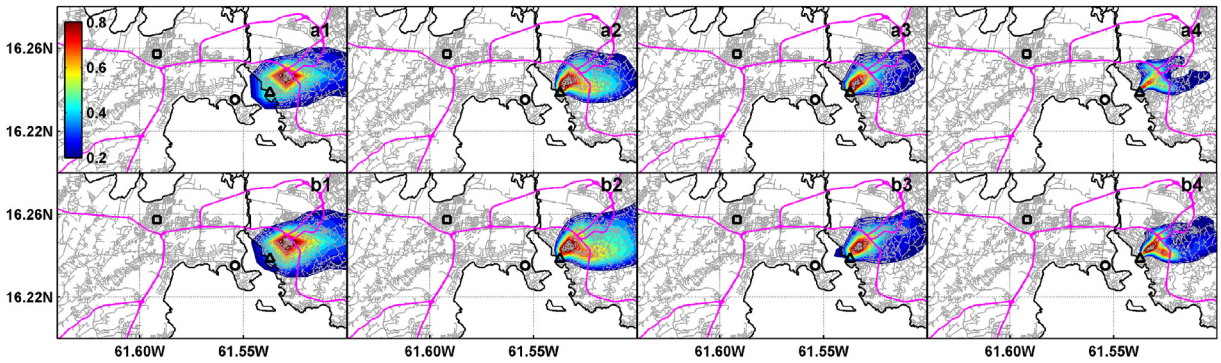

Fig. 13. 24-h backward plume from AQS1 location 2330 LT 03 Dec with normalized residence time vertically integrated between 50 and 200 m AGL (a1–a3) and integrated between 100 and 300 m AGL (b1–b3); (a1,b1) FLEXPART-1km-YSU, (a2,b2)) FLEXPART-333m-YSU, (a3,b3) FLEXPART-333m-LES, (a4,b4) FLEXPART-111m-LES; with AQS1 (triangle), AQS2 (square), PWP (circle), PRN (magenta line) and the secondary road network (grey lines). (For interpretation of the references to color in this figure legend, the reader is referred to the web version of this article.)

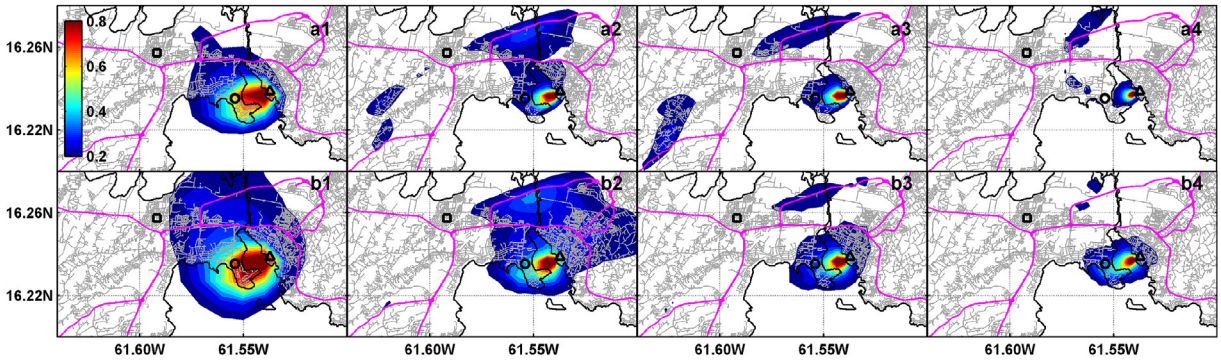

Fig. 14. 24-h backward plume from AQS1 location 0715 LT 04 Dec with normalized residence time vertically integrated between 50 and 200 m AGL (a1–a3) and integrated between 100 and 300 m AGL (b1–b3); (a1,b1) FLEXPART-1km-YSU, (a2,b2)) FLEXPART-333m-YSU, (a3,b3) FLEXPART-333m-LES, (a4,b4) FLEXPART-111m-LES; with AQS1 (triangle), AQS2 (square), PWP (circle), PRN (magenta line) and the secondary road network (grey lines). (For interpretation of the references to color in this figure legend, the reader is referred to the web version of this article.)

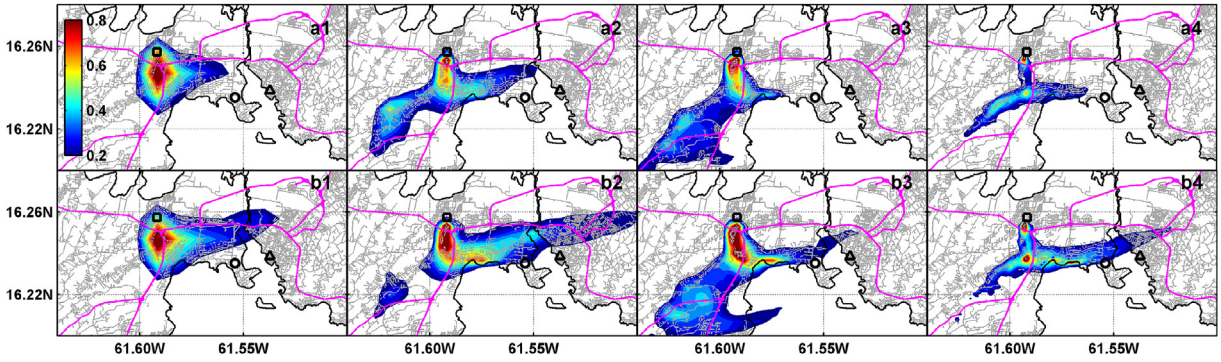

Fig. 15. 24-h backward plume from AQS2 location 2215 LT 03 Dec with normalized residence time vertically integrated between 50 and 200 m AGL (a1–a3) and integrated between 100 and 300 m AGL (b1–b3); (a1,b1) FLEXPART-1km-YSU, (a2,b2)) FLEXPART-333m-YSU, (a3,b3) FLEXPART-333m-LES, (a4,b4) FLEXPART-111m-LES; with AQS1 (triangle), AQS2 (square), PWP (circle), PRN (magenta line) and the secondary road network (grey lines). (For interpretation of the references to color in this figure legend, the reader is referred to the web version of this article.)

particle accumulation in the transition layer between the first 200-m levels westerly downslope flow and the upper levels easterly trade winds (Fig. 16b4).

4. Summary and conclusions

The main goal of this study was to analyze how microscale resolutions affect air pollution modelling in a small tropical island during a real case of weak trade winds. Three resolutions of domain grid have been selected: 1 km, 333 m and 111 m. The WRF-LES model was used to produce real nested microscale meteorological fields starting from 6-h global analysis data with a resolution of 1°. In order to dissociate the resolution effects from the turbulence scheme effects in the “turbulence grey zone”, an additional 333-m grid simulation was made with the ensemble-mean YSU scheme. Then the WRF-1km-YSU, WRF-333m-YSU, WRF-333m-LES and

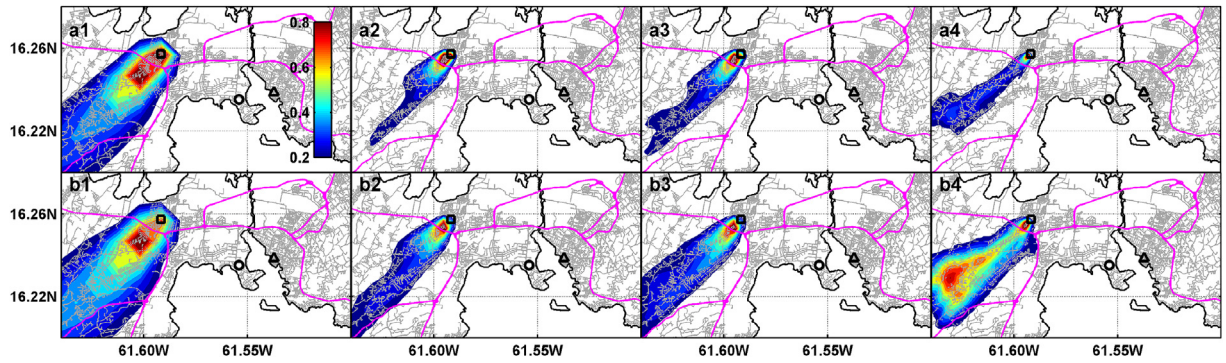

Fig. 16. 24-h backward plume from AQS2 location 0730 LT 04 Dec with normalized residence time vertically integrated between 50 and 200 m AGL (a1–a3) and integrated between 100 and 300 m AGL (b1–b3); (a1,b1) FLEXPART-1km-YSU, (a2,b2)) FLEXPART-333m-YSU, (a3,b3) FLEXPART-333m-LES, (a4,b4) FLEXPART-111m-LES; with AQS1 (triangle), AQS2 (square), PWP (circle), PRN (magenta line) and the secondary road network (grey lines). (For interpretation of the references to color in this figure legend, the reader is referred to the web version of this article.)

WRF-111m-LES weather outputs initialized the Lagrangian Particle Dispersion Model FLEXPART with an interval time of 10 min. The present study was focused on NO_x air pollution in the densely populated area of the Guadeloupe archipelago, during a typical day of severe pollution. In this area, the two main sources of NO_x are the power plant PWP and the primary road network PRN. The forward dispersion of the PWP plume was first analyzed to determine risk areas for people. Then, peaks recorded by two air quality stations have been backward simulated to identify their source.

For the three resolutions, the forward simulations with a history interval of 15 min, show good ability to reproduce nocturnal peaks recorded by the urban air quality station AQS1 which is located at 1.7 km from the power plant PWP. The increase in resolution resulted in an improvement of model sensitivity. However, the model tends globally to overestimate these NO_x peaks. The nesting to subkilometer grids helps to reduce the MAE by 9 $\mu g\ m^{-3}$ and the use of the LES scheme in the 333-m grid domain allows to decrease it by 3 $\mu g\ m^{-3}$. LES domains better simulate turbulent motions governing the pollution dispersion in the convergence area between the westerly downslope flow and the easterly land-breeze. The current overestimation error could also be linked with the approximate emitted total mass (i.e. annual mean) which would be larger than reality.

For the two peaks observed at each station, AQS1 and AQS2, the backward sensitivity outputs identified the two realistic sources of NO_x in the area: PWP and PRN. Globally, the increase in resolution helps to produce sharper inverse-plume with a more accurate source area. In some cases, while the 1-km resolution outputs identify the road PRN as the only source, the FLEXPART-333m-YSU, FLEXPART-333m-LES and FLEXPART-111m-LES outputs show the additional contribution of the power plant PWP.

This study showed the first application of the FLEXPART-WRF model to microscale resolutions. Overall, the coupling model WRF-LES-FLEXPART is useful to simulate the pollutant dispersion during a real case of calm wind regime over a complex terrain area. The forward and backward simulation results showed clearly that the subkilometer resolution of 333 m is necessary to reproduce realistic air pollution patterns in this case of short-range transport over a complex terrain area. The simulation results also indicated that at this scale (i.e., 333 m) corresponding to the "turbulence grey zone", the 3D Large Eddy Simulation scheme is needed to improve the simulated forward concentrations while the YSU 1D ensemble-mean turbulence scheme may be used to identify sources of pollution. The LES nesting from the 333-m to 111-m resolution allows to slightly improve the accuracy of air pollution fields and to better simulate near-source high concentration areas.

The present results need to be validated with more observational data recorded by air quality stations closer to the potential NO_x sources in the archipelago. In order to improve the particles dispersion modelling at microscale resolution, the FLEXPART turbulence schemes using the WRF turbulent kinetic energy, need to be tested. This first study dealing with realistic microscale air pollution modelling over a small tropical island offers prospects for applications to anthropogenic sources and other local emission sources (e.g., H2S gas released by coastal sargassum seaweed, volcano plume and fumaroles) affecting the air quality of the Lesser Antilles islands.

Globally, this work contributes to enrich the sparsely documented domain of real nested microscale air pollution modelling. This study dealing with the determination of the proper resolution grid and proper turbulence scheme, is of significant interest to the near-source and complex terrain air quality research community. The comparison between resolutions and turbulence schemes would also help the FLEXPART-WRF users to optimize the computational costs which restrict operational applications. The present approach may be used as a decision tool for policy-makers; it can be applied to near-source and complex terrain cases to predict associated risks for the population health.

Acknowledgments

This study was supported by the Research Laboratory in Geosciences and Energy (LaRGE, University of the French West Indies, Guadeloupe) and the Direction of Environment, Development and Housing (DEAL Guadeloupe). The author is thankful to the Air Quality Agency of Guadeloupe (Gwadair) for providing observational data recorded from AQS1 and AQS2. The weather observational data from WS2 were obtained from the French Met Office (Météo France). The authors gratefully acknowledge Dr. C. d'Alexis for providing the 1-Hz weather observational data recorded from WS1. The WRF simulations were computed on the Wahoo cluster [Intensive Computing Center (C3I), University of the French West Indies] thanks to engineer Raphaël Pasquier. The authors wish to thank Danièle Frison who helped with the translation.

Appendix A

The statistical tools used in the present study are widely used in numerical studies (Cécé et al., 2014). Firstly, individual model-prediction errors are defined as $e_i = P_i - O_i$ ($i = 1,2,\ldots,n$), where P_i and O_i are respectively model predictions and in situ observations. The mean bias error is defined as $\mathrm{MBE} = n^{-1}\sum_{i=1}^{n} e_i = \overline{P} - \overline{O}$. The

mean absolute error is written as $\mathrm{MAE} = n^{-1}\sum_{i=1}^{n}\left|e_i\right|$. Willmott et al. (2012) developed index of agreement (with the value range of [−1, 1]), correlated with MAE variations. This index is expressed as

$$\mathrm{IOA} = \begin{cases} 1 - \dfrac{\sum_{i=1}^{n}\left|e_i\right|}{2\sum_{i=1}^{n}\left|O_i - \overline{O}\right|}, \text{when} \sum_{i=1}^{n}\left|e_i\right| \le 2\sum_{i=1}^{n}\left|O_i - \overline{O}\right| \\ \dfrac{2\sum_{i=1}^{n}\left|O_i - \overline{O}\right|}{\sum_{i=1}^{n}\left|e_i\right|} - 1, \text{when} \sum_{i=1}^{n}\left|e_i\right| > 2\sum_{i=1}^{n}\left|O_i - \overline{O}\right| \end{cases} \quad (2)$$

As in Cécé et al. (2014), a value of IOA of 0.5, indicates that the sum of error-magnitudes is one half of the sum of perfect-model-deviation and observed-deviation magnitudes. On the other hand, a value of IOA2 of −0.5, means that the sum of error-magnitudes is twice the sum of the perfect-model-deviation and observed-deviation magnitudes.

References

Anderson, J.R., Hardy, E.E., Roach, J.T., Witmer, R.E., 1976. A Land Use and Land Cover Classification System for Use with Remote Sensor Data. Technical Report Geological Survey Professional Paper 964.

Angevine, W.M., Brioude, J., McKeen, S., Holloway, J.S., Lerner, B.M., Goldstein, A.H., Abhinav, Guha, Andrews, A., Nowak, J.B., Evan, S., Fischer, M.L., Gilman, J.B., Bon, D., 2013. Pollutant transport among California regions. J. Geophys. Res. 118, 6750–6763.

Brévignon, C., 2003. Atlas climatique: l'environnement atmosphérique de la Guadeloupe, de Saint-Barthélémy et Saint-Martin. Météo-France, Service Régional de Guadeloupe.

Brioude, J., Stohl, A., Cassiani, M., Morton, D., Seibert, P., Angevine, W., Evan, S., Dingwell, A., Fast, J.D., Easter, R.C., Pisso, I., Burkhart, J., Wotawa, G., 2013. The Lagrangian particle dispersion model FLEXPART-WRF. Geosci. Model Dev. 6, 1889–1904.

Carlis, D.L., Chen, Y.-L., Morris, V.R., 2010. Numerical simulations of island-scale airflow over Maui and the Maui vortex under summer trade wind conditions. Mon. Wea. Rev. 138, 2706–2736.

Cécé, R., Bernard, D., d'Alexis, C., Dorville, J.-F., 2014. Numerical simulations of island-induced circulations and windward katabatic flow over the Guadeloupe Archipelago. Mon. Wea. Rev. 142, 850–867.

Chen, F., Dudhia, J., 2001. Coupling an advanced land surface-hydrology model with the Penn State-NCAR MM5 modeling system. Part I: model implementation and sensitivity. Mon. Wea. Rev. 129, 569–585.

Chu, X., Xue, L., Geerts, B., Rasmussen, R., Breed, D., 2014. A case study of radar observations and WRF LES simulations of the impact of ground-based glaciogenic seeding on orographic clouds and precipitation. Part I: observations and model validations. J. Appl. Meteor. Climatol. 53, 22642286.

D'Alexis, C., Abouna, A., Berthelot, H., Bernard, D., 2011. Characteristics of nocturnal breezes in the windward islands in the southeastern Caribbean: structure and nighttime regimes. e-J. Caribb. Acad. Sci. 5.

Dudhia, J., 1989. Numerical study of convection observed during the winter monsoon experiment using a mesoscale two-dimensional model. J. Atmos. Sci. 46, 3077–3107.

EEA, 2007. CLC2006 Technical Guidelines (Technical Report European Environment Agency).

de Foy, B., Zavala, M., Bei, N., Molina, L.T., 2009. Evaluation of WRF mesoscale simulations and particle trajectory analysis for the MILAGRO field campaign. Atmos. Chem. Phys. 9, 4119–4438.

Hanna, S.R., 1982. Applications in air pollution modeling. In: Nieuwstadt, F.T.M., van Dop, H. (Eds.), Atmospheric Turbulence and Air Pollution Modelling. D. Reidel Publishing Company, Dordrecht, Holland.

Heo, J., de Foy, B., Olson, M.R., Pakbin, P., Sioutas, C., Schauer, J.J., 2015. Impact of regional transport on the anthropogenic and biogenic secondary organic aerosols in the Los Angeles basin. Atmos. Environ. 103, 171–179.

Hong, S.-Y., Lim, J.-O.J., 2006. The WRF single-moment 6-class microphysics scheme (WSM6). J. Korean. Meteor. Soc. 42, 129–151.

Hong, S.-Y., Noh, Y., Dudhia, J., 2006. A new vertical diffusion package with an explicit treatment of entrainment processes. Mon. Wea. Rev. 134, 2318–2341.

Honnert, R., Masson, V., Couvreux, F., 2011. A diagnostic for evaluating the representation of turbulence in atmospheric models at the kilometric scale. J. Atmos. Sci. 68, 31123131.

Hu, X.-M., Klein, P.M., Xue, M., 2013. Evaluation of the updated YSU planetary boundary layer scheme within WRF for wind resource and air quality assessments. J. Geophys. Res. 118, 10,490–10,505.

Hu, X.-M., Nielsen-Gammon, J.W., Zhang, F., 2010. Evaluation of three planetary boundary layer schemes in the WRF model. J. Appl. Meteor. 49, 1831–1844.

Jähn, M., Muñoz-Esparza, D., Chouza, F., Reitebuch, O., 2015. Investigations of boundary layer structure, cloud characteristics and vertical mixing of aerosols at Barbados with large eddy simulations. Atmos. Chem. Phys. Discuss. 15, 22637–22699.

Joe, D.K., Zhang, H., DeNero, S.P., Lee, H.-H., Chen, S.-H., McDonald, B.C., Harley, R.A., Kleeman, M.J., 2014. Implementation of a high-resolution source-oriented WRF/chem model at the Port of Oakland. Atmos. Environ. 82, 351–363.

Jury, M.R., Chiao, S., Harmsen, E.W., 2009. Mesoscale structure of trade wind convection over Puerto Rico: composite observations and numerical simulation. Bound. Layer. Meteor. 132, 289–313.

Kain, J.S., 2004. The Kain-Fritsch convective parameterization: an update. J. Appl. Meteor. 43, 170–181.

Lefèvre, J., Marchesiello, P., Jourdain, N.C., Menkes, C., Leroy, A., 2010. Weather regimes and orographic circulation around New Caledonia. Mar. Pollut. Bull. 61, 413–431.

Lesouëf, D., Gheusi, F., Delmas, R., Escobar, J., 2011. Numerical simulations of local circulations and pollution transport over Reunion Island. Ann. Geophys. 29, 53–69.

Lilly, D.K., 1967. The representation of small-scale turbulence in numerical simulation experiments. In: IBM Scientific Computing Symp. on Environmental Sciences 320-1951. IBM, White Plains, NY, USA.

Liu, Y., Warner, T., Liu, Y., Vincent, C., Wu, W., Mahoney, B., Swerdlin, S., Parks, K., Boehnert, J., 2010. Simultaneous nested modeling from the synoptic scale to the LES scale for wind energy applications. In: The Fifth Int. Symposium on Computational Wind Engineering (p. 8). Chapel Hill, North Carolina, USA.

Lundquist, J.K., Mirocha, J.D., Kosovic, B., 2010. Nesting large-eddy simulations within mesoscale simulations in WRF for wind energy applications. In: The Fifth Int. Symposium on Computational Wind Engineering (p. 6). Chapel Hill, North Carolina, USA.

Madalaa, S., Satyanarayana, A., Srinivas, C.V., Kumar, M., 2015. Mesoscale atmospheric flow-field simulations for air quality modeling over complex terrain region of Ranchi in eastern India using WRF. Atmos. Environ. 107, 315–328.

Mahrer, Y., Pielke, R.A., 1976. Numerical simulation of the airflow over Barbados. Mon. Wea. Rev. 104, 1392–1402.

Marjanovic, N., Chow, F.K., Lundquist, J.K., 2010. Nested mesoscale to large-eddy simulations for wind energy applications. In: The Fifth Int. Symposium on Computational Wind Engineering (p. 8). Chapel Hill, North Carolina, USA.

Matthews, S., Hacker, J.M., Cole, J., Hare, J., Long, C.N., Reynolds, R.M., 2007. Modification of the atmospheric boundary layer by a small island: observations from Nauru. Mon. Wea. Rev. 135, 891–905.

Mirocha, J., Kirkil, G., 2010. Nested high-resolution mesoscale/large eddy simulations in WRF: challenges and opportunities. In: The Fifth Int. Symposium on Computational Wind Engineering (p. 8). Chapel Hill, North Carolina, USA.

Mirocha, J., Kosović, B., Kirkil, G., 2014. Resolved turbulence characteristics in large-eddy simulations nested within mesoscale simulations using the weather research and forecasting model. Mon. Wea. Rev. 142, 806–831.

Mlawer, E.J., Taubman, S.J., Brown, P.D., Iacono, M.J., Clough, S.A., 1997. Radiative transfer for inhomogeneous atmosphere: RRTM, a validated correlated-k model for the longwave. J. Geophys. Res. 102, 16663–16682.

Moeng, C.-H., Dudhia, J., Klemp, J., Sullivan, P., 2007. Examining two-way grid nesting for large eddy simulation of the PBL using the WRF model. Mon. Wea. Rev. 135, 2295–2311.

Muñoz-Esparza, D., Kosović, B., Mirocha, J., van Beek, J., 2014. Bridging the transition from mesoscale to microscale turbulence in numerical weather prediction models. Bound. Layer Meteorol. 153, 409–440.

Nguyen, H.V., Chen, Y.-L., Fujioka, F., 2010. Numerical simulations of island effects on airflow and weather during the summer over the island of Oahu. Mon. Wea. Rev. 138, 2253–2280.

Oliphant, A.J., Sturman, A.P., Tapper, N.J., 2001. The evolution and structure of a tropical island sea/land-breeze system, northern Australia. Meteor. Atmos. Phys. 78, 45–59.

Pineda, N., Jorba, O., Jorge, J., Baldasano, J.M., 2004. Using NOAA AVHRR and SPOT VGT data to estimate surface parameters: application to a mesoscale meteorological model. Int. J. Remote Sens. 25, 129–143.

Plocoste, T., Jackoby-Koaly, S., Molinié, J., Petit, R.H., 2014. Evidence of the effect of an urban heat island on air quality near a landfill. Urban Clim. 10, 745–757.

Poulidis, A., Renfrew, I., Matthews, A., 2016. Thermally induced convective circulation and precipitation over an isolated volcano. J. Atmos. Sci. 73, 1667–1686.

Sandeepan, B.S., Rakesh, P.T., Venkatesan, R., 2013. Numerical simulation of observed submesoscale plume meandering under nocturnal drainage flow. Atmos. Environ. 69, 29–36.

Seaman, N.L., Gaudet, B.J., Stauffer, D.R., Mahrt, L., Richardson, S.J., Zielonka, J.R., Wyngaard, J.C., 2012. Numerical prediction of submesoscale flow in the nocturnal stable boundary layer over complex terrain. Mon. Wea. Rev. 140, 956–977.

Shin, H.H., Hong, S.-Y., 2011. Intercomparison of planetary boundary-layer parametrizations in the WRF model for a single day from CASES-99. Bound. Layer Met. 139, 261–281.

Skamarock, W.C., Klemp, J.B., Dudhia, J., Gill, D.O., Barker, D.M., Duda, M.G., Huang, X.-Y., Wang, W., Powers, J.G., 2008. A Description of the Advanced Research WRF Version 3 (Technical Report National Center for Atmospheric Research).

Smith, R.B., Gleason, A.C., Gluhosky, P.A., 1997. The wake of St. Vincent. J. Atmos. Sci. 54, 606–623.

Smith, R.B., Minder, J.R., Nugent, A.D., Storelvmo, T., Kirshbaum, D.J., Warren, R., Lareau, N., Palany, P., James, A., French, J., 2012. Orographic precipitation in the tropics: the Dominica experiment. Bull. Amer. Meteor. Soc. 93, 1567–1579.
Srinivas, C.V., Prasad, K.B.R.R.H., Naidu, C.V., Baskaran, R., Venkatraman, B., 2015. Sensitivity analysis of atmospheric dispersion simulations by FLEXPART to the WRF- simulated meteorological predictions in a coastal environment. Pure Appl. Geophys. 1–26.
Stohl, A., Foster, C., Frank, A., Seibert, P., Wotawa, G., 2005. Technical note: the Lagrangian particle dispersion model FLEXPART version 6.2. Atmos. Chem. Phys. 5, 2461–2474.
Talbot, C., Bou-Zeid, E., Smith, J., 2012. Nested mesoscale large-Eddy simulations with WRF: performance in real test cases. J. Hydrometeor. 13, 1421–1441.
Whitehall, K., Chiao, S., Mayers-Als, M., 2013. Numerical investigations of convective initiation in Barbados. Adv. Meteorol. 2013, 10.
Willmott, C.J., Robeson, S.M., Matsuura, K., 2012. A refined index of model performance. Int. J. Climatol. 32, 20882094.
Wyngaard, J.C., 2004. Toward numerical modeling in the “terra incognita”. J. Atmos. Sci. 61, 1816–1826.
Yang, Y., Chen, Y.-L., 2005. Numerical simulations of the island-induced circulations over the island of Hawaii during HaRP. Mon. Wea. Rev. 133, 3693–3713.
Yu, N., Barthe, C., Plu, M., 2014. Evaluating intense precipitation in high-resolution numerical model over a tropical island: impact of model horizontal resolution. Nat. Hazards Earth Syst. Sci. Discuss. 2, 999–1032.
Zhu, P., 2008a. A multiple scale modeling system for coastal hurricane wind damage mitigation. Nat. Hazards 47, 577–591.
Zhu, P., 2008b. Simulation and parameterization of the turbulent transport in the hurricane boundary layer by large eddies. J. Geophys. Res. 113.